

WHAT DETERMINES THE LOCAL METALLICITY OF GALAXIES: GLOBAL STELLAR MASS, LOCAL STELLAR MASS SURFACE DENSITY OR STAR FORMATION RATE?

YULONG GAO^{1,2}, ENCI WANG^{1,2,3}, XU KONG^{1,2}, ZESEN LIN^{1,2}, GUILIN LIU^{1,2}, HAIYANG LIU^{1,2}, QING LIU^{1,2}, NING HU^{1,2},
 BERZAF BERHANE TEKLU^{1,2}, XINKAI CHEN^{1,2}, AND QINYUAN ZHAO^{1,2}

¹ CAS Key Laboratory for Research in Galaxies and Cosmology, Department of Astronomy, University of Science and Technology of China, Hefei 230026, China; ylgao@mail.ustc.edu.cn, ecwang16@ustc.edu.cn, xkong@ustc.edu.cn

² School of Astronomy and Space Sciences, University of Science and Technology of China, Hefei 230026, China

³ Department of Physics, Institute for Astronomy, ETH Zurich, CH-8093 Zurich, Switzerland

Draft version October 23, 2018

ABSTRACT

The metallicity and its relationship with other galactic properties is a fundamental probe of the evolution of galaxies. In this work, we select about 750,000 star-forming spatial pixels from 1122 blue galaxies in the MaNGA survey to investigate the global stellar mass – local stellar mass surface density – gas-phase metallicity ($M_* - \Sigma_* - Z$) relation. At a fixed M_* , the metallicity increases steeply with increasing Σ_* . Similarly, at a fixed Σ_* , the metallicity increases strongly with increasing M_* at low mass end, while this trend becomes less obvious at high mass end. We find the metallicity to be more strongly correlated to Σ_* than to M_* . Furthermore, we construct a tight (0.07 dex scatter) $M_* - \Sigma_* - Z$ relation, which reduces the scatter in the $\Sigma_* - Z$ relation by about 30% for galaxies with $7.8 < \log(M_*/M_\odot) < 11.0$, while the reduction of scatter is much weaker for high-mass galaxies. This result suggests that, especially for low-mass galaxies, the $M_* - \Sigma_* - Z$ relation is largely more fundamental than the $M_* - Z$ and $\Sigma_* - Z$ relations, meaning that both M_* and Σ_* play important roles in shaping the local metallicity. We also find that the local metallicity is probably independent on the local star formation rate surface density at a fixed M_* and Σ_* . Our results are consistent with the scenario that the local metallicities in galaxies are shaped by the combination of the local stars formed in the history and the metal loss caused by galactic winds.

Keywords: galaxies: abundances - galaxies: evolution - galaxies: starburst - star formation

1. INTRODUCTION

The chemical processes of the gas and stars in galactic environments is of key importance in understanding the formation and evolution of galaxies, and the metallicity of the interstellar medium (Z), along with its relationship with other galactic properties, is a fundamental probe. The observed metallicity is a result of the interplay between the enrichment from previous generations of stars, the metal loss caused by winds from stars and active galactic nuclei (AGN), and the dilution by metal-poor gas inflows. In spite of the investigation for the chemical evolution is complex, the scaling relations between metallicity and other galactic properties provides a powerful alternative approach.

Since its establishment by Lequeux et al. (1979), the relation between stellar mass and metallicity has been studied for decades (e.g. Garnett & Shields 1987; Tremonti et al. 2004). It is a positive correlation, meaning that the metallicities of galaxies increase with increasing stellar masses. The significant scatter in the stellar mass – metallicity relation (MZR) implies the complication of the underlying physical and chemical processes in an evolving galaxy. Variations in galactic parameters, such as the star formation rate (SFR), the 4000 Å break (D_n4000), and the galaxy size and morphology, are found to contribute to the scatter in MZR (e.g. Ellison et al. 2008; Mannucci et al. 2010; Yates et al. 2012; Andrews & Martini 2013; Lian et al. 2015; Bothwell et al. 2016; Wang et al. 2018). In particular, using the SDSS Data Release (DR) 7 (Abazajian et al. 2009), Mannucci et al. (2010) and Andrews & Martini (2013) found

that metallicity to be anti-correlated with SFR at a fixed stellar mass, and the scatter in MZR is significantly suppressed when a stellar mass – SFR – metallicity relation (fundamental metallicity relation; FMR) is constructed. Nevertheless, with the same data SDSS DR7, Salim et al. (2014) argued that a more physically motivated second parameter for the MZR is the specific SFR (sSFR) when $\log(M_*/M_\odot) \leq 10.5$. Bothwell et al. (2016) derived the molecular hydrogen masses from the CO luminosity for 221 galaxies at $0 < z < 2$, then suggested that instead of the SFR, the third parameter that should be introduced into FMR is the gas mass.

The MZR and FMR are both established primarily using global galaxy parameters, it is also important to understand whether there is a more fundamental relation to probe the global MZR or FMR with local galactic parameters, e.g. stellar mass surface density, local metallicity, local SFR and local D_n4000 . The local metallicity vs. local stellar mass surface density relation has been investigated for years. Edmunds & Pagel (1984) and Vila-Costas & Edmunds (1992) reported that H II regions with larger stellar mass densities are more metal-rich than those with lower densities. Moran et al. (2012) performed long-slit spectroscopy on 174 star-forming galaxies and found a correlation between the local stellar mass surface density and metallicity, an analog to the global MZR. More recently, thanks to the emergence of the integral field spectroscopy (IFS) technique, analyzing these relations in a spatially resolved manner in relatively large samples of galaxies becomes feasible. Rosales-Ortega et al. (2012) demonstrated the existence of a local rela-

tion between stellar mass surface density, metallicity, and SFR density using 38 nearby galaxies from the PINGS survey (Rosales-Ortega et al. 2010) and the CALIFA survey (Sánchez et al. 2012). Based on the SDSS-IV MaNGA survey (Bundy et al. 2015; Yan et al. 2015, 2016; Blanton et al. 2017), Barrera-Ballesteros et al. (2016) and Zhu et al. (2017) presented a tight local stellar mass surface density versus metallicity relation, suggestive of the fact that local properties play a key role in determining the metallicity in typical disk galaxies. These authors also reproduced the global MZR using the local relation, concluding that the global relation is a scale-up, integrated effect of the local relation. In addition, a series of studies with IFS data explored whether there is a secondary dependent parameter in the global MZR or the stellar mass surface density – metallicity relation. Using the data in CALIFA survey, Sánchez et al. (2013) and Sánchez et al. (2017) presented the local mass surface density – metallicity relation and global MZR, and confirmed the nonexistence of such these relations with (s)SFR. Barrera-Ballesteros et al. (2017) also demonstrated that the MZR is independent on the (s)SFR with more than 1700 galaxies in MaNGA survey.

It is well known that the global stellar mass dominates the metallicity in the center of galaxies (Tremonti et al. 2004; Mannucci et al. 2010). However, it remains unclear whether the global stellar mass has a nonnegligible effect on shaping the distribution of local metallicity. Intuitively, higher global stellar mass helps producing deeper gravitational potential wells in a massive galaxy that retain the metals (re)processed by stars, possibly leading to a higher local metallicity than in a less massive galaxy, even if these galaxies have an identical surface density distribution of stellar mass. Barrera-Ballesteros et al. (2016) have found that the stellar mass surface density and metallicity relation is largely independent on the total stellar mass for massive ($\log(M_*/M_\odot) \geq 9.5$) galaxies. In this work, we will investigate whether the global stellar mass, especially for low-mass galaxies, is a potential parameter that participates in controlling local metallicity, and to construct a correlation between global stellar mass, local stellar mass surface density and local metallicity, in order to shed light on understanding the local chemical evolution history in galaxies.

The remainder of this paper is organized as follows. In Section 2, we present the sample selection for star-forming galaxies, the methodology for detecting and measuring nebular emission lines, and the determination of dust attenuation properties, gas-phase oxygen abundances and other galaxy parameters. In Section 3, we describe the methods for estimating the strength of the correlation between $M_* - Z$ and $\Sigma_* - Z$, as well as that of a new $M_* - \Sigma_* - Z$ relation. We discuss our results in the context of the literature, and the dependence of the residuals on other parameters in Section 4. Finally, we summarize our results in Section 5. Throughout this paper, we adopt a flat Λ CDM cosmology with $\Omega_\Lambda = 0.7$, $\Omega_m = 0.3$, and $H_0 = 70 \text{ km s}^{-1} \text{ Mpc}^{-1}$.

2. DATA ANALYSIS

2.1. MaNGA Overview

The MaNGA (Mapping Nearby Galaxies at Apache Point Observatory) survey, one of the three core pro-

grams in the Sloan Digital Sky Survey IV (SDSS-IV, Blanton et al. 2017), is an IFS survey aiming at 10,000 nearby galaxies that are selected from the NASA-Sloan-Atlas (NSA) catalog¹ (Blanton et al. 2011; Bundy et al. 2015). The redshift of these target galaxies span a range of $0.01 < z < 0.15$. The spectrographs of the MaNGA survey provide a spectral coverage of 3600 – 10300 Å at a resolution of $R \sim 2000$ (Drory et al. 2015). The diameter of an individual fiber is 2". SDSS DR14 (Abolfathi et al. 2018), the second data release of MaNGA, has delivered a public sample of 2812 galaxies with spatially resolved IFS mapping². In this work, we treat these 2812 galaxies as the parent sample.

2.2. Spectral Fitting And Emission-line Measurements

In general, one needs to disintegrate the emission lines from the underlying stellar continuum, and then measure the fluxes of these lines (Hu et al. 2016; Gao et al. 2017). For strong emission lines, the subtraction of the stellar continuum has negligible effect on the flux measurements. In this work, this decomposition is performed using the STARLIGHT code (Cid Fernandes et al. 2005). We fit each spectrum with the combination of 45 single stellar populations (SSPs) from Bruzual & Charlot (2003) model, assume a Chabrier (2003) initial mass function (IMF), and obtain the stellar population parameters. These SSPs are evenly distributed on an age – metallicity grid, which consists of 15 ages (ranging from 1 Myr to 13 Gyr) and 3 different metallicities ($Z = 0.01, 0.02, 0.05$). We also mask out optical emission lines using the standard emission line masks of STARLIGHT.

Before the spectral fitting, these spectra all have been corrected for Galactic extinction using the color excess $E(B - V)$ map of the Milky Way (Schlegel et al. 1998), and the Calzetti et al. (2000) attenuation law is adopted for correcting their intrinsic stellar reddening. We calculate the fluxes of the strong emission lines (e.g. $[\text{O II}]\lambda 3727$, $[\text{O III}]\lambda 4363$, $\text{H}\beta$, $[\text{O III}]\lambda\lambda 4959, 5007$, $\text{H}\alpha$, $[\text{N II}]\lambda\lambda 6548, 6583$, $[\text{S II}]\lambda\lambda 6717, 6731$) by fitting their profiles to multiple Gaussians using the IDL package MPFIT (Markwardt et al. 2009). The signal-to-noise ratios (S/N) of these emission lines are estimated following Ly et al. (2014).

Comparing the Balmer decrement (e.g. $\text{H}\alpha/\text{H}\beta$ ratio) to their intrinsic values that can be theoretically calculated under the “Case B” assumption, one could derive the dust attenuation (the dust geometry is postulated to be a non-scattering screen at a distance from the emitter, see Liu et al. (2013) for discussion on the complication of the dust geometry in galaxies). The Balmer decrement is insensitive to the temperature and electron density, and here we adopt a intrinsic flux ratio of $(\text{H}\alpha/\text{H}\beta)_0 = 2.86$ (Hummer & Storey 1987). We use the Calzetti et al. (2000) reddening formalism to derive the color excesses $E(B - V)$, and correct for the dust extinction for the emission line fluxes. When the observed flux ratio is unphysically $\text{H}\alpha/\text{H}\beta < 2.86$ (due to error scatter), we set $E(B - V)$ to zero in an ad hoc manner.

2.3. Sample Selection

¹ <http://www.nsatlas.org>

² <http://www.sdss.org/dr14/manga/manga-data/catalogs>

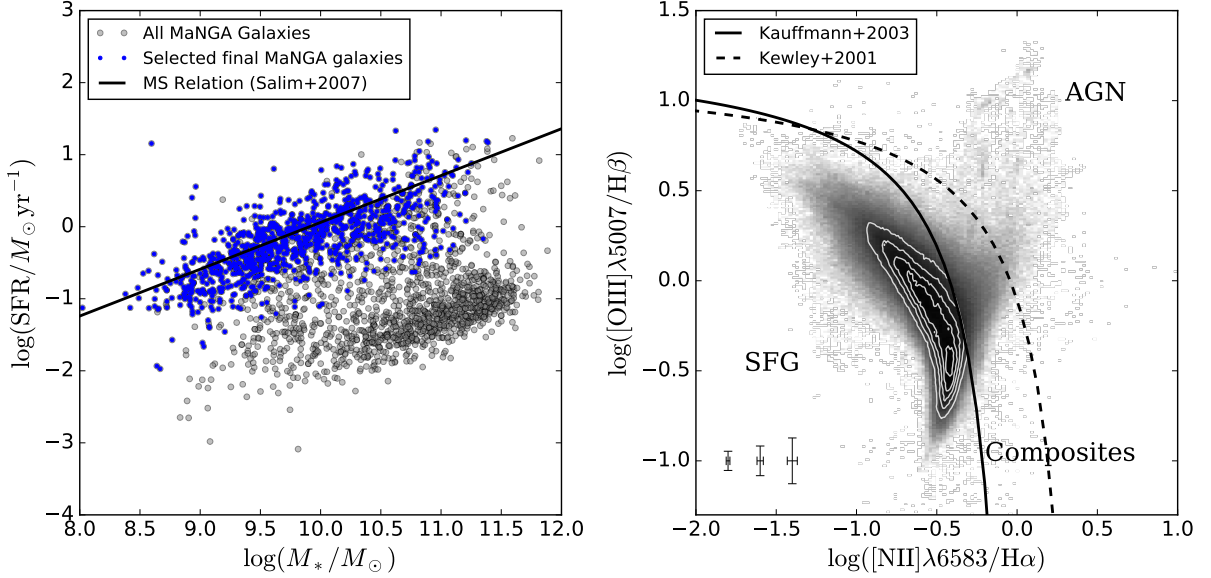


Figure 1. *Left:* The total stellar mass – SFR (main sequence) relation for MaNGA galaxies. The blue points represent our final 1122 sample galaxies, while the grey points show all of the galaxies in MaNGA data. The main sequence relation for star-forming galaxies in local universe (Salim et al. 2007; Speagle et al. 2014) is shown as the black solid line. *Right:* The BPT diagram for all spaxels in our sample blue galaxies. The grayscale 2D histogram shows the number density of observations. The white contours cover the 85% of our final sample spaxels. The solid and dashed lines are the demarcation curves between SFGs and AGNs defined by Kauffmann et al. (2003) and Kewley et al. (2001), respectively. The errorbars in the left bottom corner represent the error values at the distribution of 16%, 50% and 84%, respectively.

We retrieve the photometry of these 2812 galaxies from the NSA catalog. Since the metallicity under consideration is gas-phase metallicity, we focus on the star-forming galaxies with $\text{NUV} - r < 4$ (Li et al. 2015), whose metallicities can be reliably measured. Due to the same reason, we only consider the H II regions of the selected galaxies, confining the spatial pixels (a.k.a. “spaxels”) to those with $\text{S/N}(\text{H}\alpha) > 5$, $\text{S/N}(\text{H}\beta) > 5$, $\text{S/N}([\text{O III}]\lambda 3727) > 5$, $\text{S/N}([\text{O III}]\lambda \lambda 4959, 5007) > 5$, $\text{S/N}([\text{N II}]\lambda 6583) > 3$ and equivalent width (EW) of $\text{H}\alpha$ larger than 10 Å. Meanwhile, in order to obtain reliable stellar mass surface density, we select the spectra with a continuum S/N higher than 3 at 5500 Å. We exclude the spaxels affected by the active galactic nucleus (AGN) using the Kauffmann et al. (2003) demarcation line in the BPT diagram (Baldwin et al. 1981; Kewley et al. 2001; Kauffmann et al. 2003). We also exclude these galaxies, in which the selected spaxels number is less than 10% of the spaxels in this galaxy.

As a result, we achieve 1122 blue galaxies with about 750,000 useful spaxels. In Figure 1, the *left* panel shows total stellar mass – SFR (main sequence) relation for MaNGA galaxies, in which the M_* and SFR are obtained from MPA/JHU catalogue³ (Kauffmann et al. 2003; Salim et al. 2007). The blue points represent our final 1122 sample galaxies, while the grey points show all of the galaxies in MaNGA data. The main sequence relation for star-forming galaxies in local universe (Salim et al. 2007; Speagle et al. 2014) is shown as the black solid line. The *right* panel shows the BPT diagram constructed with all spaxels in our sample blue galaxies, in which the grayscale two-dimensional histogram demon-

strates the number density (crowdedness) of spaxels and the white contours cover the 85% of our final sample spaxels. The solid and dashed lines are the demarcations between star-forming galaxies (SFGs) and AGNs defined by Kauffmann et al. (2003) and Kewley et al. (2001), respectively.

2.4. Determinations of Metallicity and Other Physical Properties

The electron temperature (T_e) method is generally deemed as the most reliable approach for deriving metallicity, which is based on the ratios of faint auroral-to-nebular emission lines (Lin et al. 2017), such as $[\text{O III}]\lambda 4363/[\text{O III}]\lambda 5007$. However, only a handful of spaxels show pronounced $[\text{O III}]\lambda 4363$ lines. Besides, variety of calibrators can also be used to estimate the metallicity (Kewley & Ellison 2008). Based on the photoionization models for H II regions, these emission line ratios, like $([\text{O II}]\lambda 3727 + [\text{O III}]\lambda \lambda 4959, 5007)/\text{H}\beta$ (R23, Kobulnicky & Kewley 2004), $[\text{N II}]\lambda 6583/[\text{O II}]\lambda 3727$ (N2O2, Kewley & Dopita 2002), can be used as the calibrators to reproduce the metallicity. Some other diagnostics, like $([\text{O III}]\lambda 5007/\text{H}\beta)/([\text{N II}]\lambda 6583/\text{H}\alpha)$ and $[\text{N II}]\lambda 6583/\text{H}\alpha$ (O3N2, N2, Pettini & Pagel 2004), are calibrated by empirical fitting to the electronic temperature (T_e) method with strong-line ratios for H II regions and galaxies. However, there is a large discrepancy between the metallicities derived by different calibrators (Kehrig et al. 2013; Morisset et al. 2016). For example, compared with the N2O2 diagnostic, O3N2 and N2 almost couldn’t reproduce the super-solar oxygen abundances and will derive lower metallicities (Blanc et al. 2015; Zhang et al. 2017).

In this work, we adopt the N2O2 diagnostic to deter-

³ http://www.sdss.org/dr12/spectro/galaxy_mpa/jhu/

mine the oxygen abundances. The N2O2 index introduced in Dopita et al. (2000) and improved by Dopita et al. (2013), is defined as

$$\text{N2O2} \equiv \log\left(\frac{[\text{N II}]\lambda 6583}{[\text{O II}]\lambda\lambda 3727, 3729}\right), \quad (1)$$

and is converted to metallicity using the relation in Kewley & Dopita (2002) as

$$12 + \log(\text{O}/\text{H}) = \log(1.54020 + 1.26602 \times \text{N2O2} + 0.167977 \times \text{N2O2}^2) + 8.93, \quad (2)$$

with a typical error of 0.04 dex when $12 + \log(\text{O}/\text{H}) \geq 8.6$. In order to obtain the general results that are independent on the metallicity calibrators, we also calculate the metallicities with O3N2 and N2 indices in Appendix.

The global stellar mass M_* is retrieved from the NSA catalog (Blanton et al. 2011). In order to derive the local stellar mass surface density Σ_* , we divide the local stellar mass in each spaxel of the output from the STARLIGHT fits by its corresponding physical area, following the method in Barrera-Ballesteros et al. (2016) to correct for the inclination by applying the minor-to-major axis ratio (b/a) retrieved from the NSA catalog. The uncertainty of the local stellar mass for each spaxel is smaller than 0.11 dex when the S/N of spectrum continuum is larger than 5. Comparing our mass surface density Σ_* with the public MaNGA Pipe3D value added catalog (Sánchez et al. 2016), we note that our Σ_* is systematically lower than the Pipe3D values, with a offset of 0.539 dex with a scatter of 0.22 dex. The offset is likely due to the difference of SSP library and IMF used in Pipe3D and our work. Pipe3D adopt the Salpeter (1955) IMF, while we use the Chabrier (2003) IMF, which may cause a offset of 0.24 ± 0.13 dex (Sánchez et al. 2016). For the MaNGA data, the Pipe3D pipeline use 12 SSPs from MIUSCAT library (Vazdekis et al. 2012), covering four stellar ages (0.06, 0.2, 2.0, 17.78 Gyr) and three metallicities (0.0004, 0.02, 0.0331), while we perform the spectrum fitting with 45 SSPs from Bruzual & Charlot (2003) model by STARLIGHT, consisting of 15 ages and 3 different metallicities (see Section 2.2).

We use the $\text{H}\alpha$ emission line luminosity to determine the dust-corrected star formation rate for each spaxel, assuming a Chabrier (2003) IMF and solar metallicity. The SFR is calculated from $\text{H}\alpha$ luminosity $L(\text{H}\alpha)$ using the relation from Kennicutt (1998):

$$\text{SFR}(\text{M}_\odot \text{yr}^{-1}) = 4.4 \times 10^{-42} \times L(\text{H}\alpha)(\text{erg s}^{-1}). \quad (3)$$

We derive the effective radius R_e (R_{50}) and the radius enclosed 90% of light (R_{90}) from the NSA catalog. With the position angle (PA), b/a , right ascension (RA) and declination (DEC) in plate center, we also determine the deprojected galactocentric distance (R) for each spaxel.

3. RESULTS

3.1. Metallicity Distribution In Stellar Mass – Mass Surface Density Space

This work is centered on the dependence of the local metallicity on the global stellar mass and the local stellar mass surface density. In Figure 2, we plot the metallicity distribution for all the sample spaxels in star-forming regions as a function of the global stellar mass and the

local stellar mass surface density, respectively. For eye-guiding purposes, we divide the plotting range of the logarithms of M_* and Σ_* into five bins (M_* : 7.8, 9.2, 9.6, 10.0, 10.5, 11.0; Σ_* : 5.7, 6.4, 7.1, 7.8, 8.5, 9.2), and thus 25 bin regions in the $M_* - \Sigma_*$ space. The median metallicity for the $M_* - \Sigma_*$ bins are calculated using more than 100 spaxels.

In Figure 2, the local metallicity distribution as a function of M_* and Σ_* is shown in the *left* and *right* panels based on the N2O2 index. The blue points connected by black lines represent the median values with different M_* (or Σ_*) bins at a fixed Σ_* (or M_*) bin. The arrows in each panel point to the direction of increasing M_* or Σ_* . The contour lines represent the distribution for 85% of all the spaxels, each contour enclose the 17%, consecutively. The red dashed line in the $\Sigma_* - Z$ plot is the best-fit $\Sigma_* - Z$ relation (see details in Section 3.3).

As can be seen in this figure, the metallicity increases together with Σ_* at a certain stellar mass, and also increases with M_* at a fixed surface mass density. In star-forming galaxies, the inner regions, where the surface mass density tends to be higher, are typically more metal-rich than the outskirt. This is in agreement with the previous findings that star-forming galaxies usually have negative metallicity gradients (e.g. Zaritsky et al. 1994; Barrera-Ballesteros et al. 2016; Lin et al. 2017; Lian et al. 2018).

On the other hand, for two regions with the same Σ_* but residing in different galaxies with different M_* , the one in the more massive galaxy appears be more metal-rich than the other, mainly for these galaxies in the low-mass region ($\log(M_*/M_\odot) \leq 10.0$), presumably indicative of the effect from global stellar mass in shaping the local metallicity. This result has been interpreted as the evidence of metal loss by the galactic winds from galaxy potential wells in the literature, because more massive galaxies construct deeper potential wells and are less efficient in metal loss (e.g. Tremonti et al. 2004; Mannucci et al. 2010; Sparre & Springel 2017).

3.2. The Correlation Strength Between Stellar Mass, Stellar Mass Surface Density And Metallicity

In this section, we investigate the strength of dependence of metallicity on M_* and Σ_* , and tackle the question which one is more closely related to the local metallicity in galaxies. For a given galaxy, we radially bin the spaxels so that $\Delta R/R_e = 0.3$. We use the median values of metallicity and Σ_* in each radial bin in the analysis below (hereafter “radial bin sample”), though excluding the bins with less than 20 spaxels. Compared to using all the relevant spaxels, this strategy ensures an even weight for different galactic radii, and suppresses the effect of outliers. In addition, the metallicity and stellar distributions are roughly azimuthally symmetrical, thus the medians of Z and Σ_* in the radial bins appear representative.

Following Yang et al. (2017), we perform a partial correlation (PCOR) analysis on our data, which is deployed to measure the correlation strength between metallicity Z and M_* (or Σ_*) while controlling the effects of Σ_* (or M_*). There are three different statistical parameters in PCOR: one parametric statistic (Pearson) and two non-parametric statistics (Spearman and Kendall). The Pearson product-moment correlation coefficient is

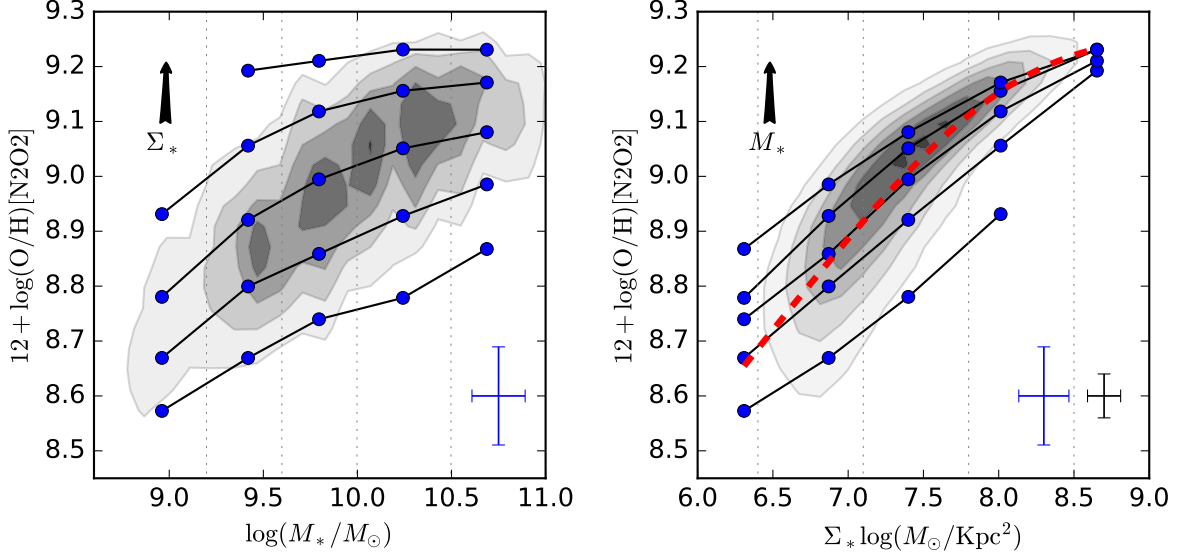


Figure 2. The metallicity distribution in M_* and Σ_* space based on N2O2 index. We divide the plotting range of the logarithms of M_* and Σ_* into five bins (M_* : 7.8, 9.2, 9.6, 10.0, 10.5, 11.0; Σ_* : 5.7, 6.4, 7.1, 7.8, 8.5, 9.2), and thus 25 bin regions in the $M_* - \Sigma_*$ space. The *left* and *right* panels show the local metallicity distribution as a function of M_* and Σ_* , respectively. Blue points connected by black lines represent the median values with different M_* (or Σ_*) bins at a fixed Σ_* (or M_*) bin. Bins with the number of spaxels less than 100 are not presented. The contour lines represent the distribution for 85% of all the spaxels, each contour enclose the 17%, consecutively. The arrow in each panel points to the direction of increasing M_* or Σ_* . The black errorbar represents the typical uncertainties in the metallicity calibration with N2O2 index and mass surface density measurement, while the blue errorbars illustrate the median values of standard deviation in the 25 bin regions. The red dashed line in $\Sigma_* - Z$ panel shows the best-fitted $\Sigma_* - Z$ relation.

a measure of the linear correlation between two variables (Pearson 1895), Spearman’s correlation coefficient is a nonparametric measure of statistical dependence between the ranking of two variables (Spearman 1904), and the Kendall correlation coefficient is used to measure the ordinal association between two measured quantities (Kendall 1938). We perform the analyses with these three statistical methods on metallicity using PCOR code⁴ in R language. The resultant significance (p values) is listed in Table 1. We find that all the p values for $M_* - Z$ and $\Sigma_* - Z$ are large, implying that metallicity have partial dependence on both M_* and Σ_* . However, we also note that all p values for the $\Sigma_* - Z$ relation are slightly larger than those for the $M_* - Z$ relation, indicating that Σ_* is more closely related to local metallicity than M_* .

3.3. The Relation Between Stellar Mass, Mass Surface Density And Metallicity

The global stellar mass – metallicity relation and stellar mass – metallicity – SFR relation have been investigated for decades (e.g. Tremonti et al. 2004; Mannucci et al. 2010; Gao et al. 2017). Previous works suppress the scatter in MZR by introducing the global SFR, finding that at a certain stellar mass, the metallicity scales up remarkably when the stellar mass increases, and scales down slightly when the SFR increases. However, the scatter in the $\Sigma_* - Z$ relation remains significant (about 0.08 dex for the O3N2 estimator) in Barrera-Ballesteros et al. (2016). In this work, we take the global stellar mass into consideration, because the metallicity also

show strong dependence on M_* , as can be seen in Figure 2.

We modify the MZR relation suggested by Moustakas et al. (2011) to the following formalism:

$$12 + \log(\text{O}/\text{H}) = 12 + \log(\text{O}/\text{H})_o - \mu_{\Sigma_*} \log[1 + (\frac{\Sigma_{\text{TO}}}{\Sigma_*})^{\gamma_{\Sigma_*}}], \quad (4)$$

where $12 + \log(\text{O}/\text{H})_o$ is the asymptotic metallicity at high stellar mass surface densities, Σ_{TO} is the turnover mass surface density, γ_{Σ_*} controls the slope of the relation at low mass surface densities, and μ_{Σ_*} is a multiplying coefficient. We apply the Equation 4 to fit our radial bin sample (Section 3.2), and list the best-fit results in Table 2. The locus of the best-fit $\Sigma_* - Z$ relation is shown with red dashed lines in Figure 2. The mean value (μ) and the standard deviation (scatter, σ) of the residuals when the predicted metallicity from the $\Sigma_* - Z$ relation is subtracted from the observed values derived from N2O2 index are also listed in Table 2. μ_{bin} and σ_{bin} represent the mean value and the scatter of the residuals for the radial bin sample, while μ_{all} and σ_{all} are the mean value and the scatter of the residuals for all spaxels, respectively.

Since the local metallicities also strongly correlate with M_* (see the upper panels in Figure 2, and p values for $M_* - Z$ in Table 1), we deduce that the remarkable scatter in the $\Sigma_* - Z$ relation may be largely contributed by the variation of the stellar mass. Introducing this ingredient, we extend the $\Sigma_* - Z$ relation (Equation 4) to the

⁴ <http://www.yilab.gatech.edu/pcor.html>

following format:

$$12 + \log(\text{O}/\text{H}) = 12 + \log(\text{O}/\text{H})_0 - \mu_{M_*} \log[1 + (\frac{M_{\text{TO}}}{M_*})^{\gamma_{M_*}}] - \mu_{\Sigma_*} \log[1 + (\frac{\Sigma_{\text{TO}}}{\Sigma_*})^{\gamma_{\Sigma_*}}], \quad (5)$$

where $12 + \log(\text{O}/\text{H})_0$ is the asymptotic metallicity at high mass and high stellar mass surface density, M_{TO} is the turnover mass, γ_{M_*} control the slope of the relation at low mass, μ_{M_*} is the coefficient. Σ_{TO} , γ_{Σ_*} and μ_{Σ_*} are the same as Equation 4. We apply the Equation 5 to fit our radial bin sample, and list the best-fitted results in Table 2. As shown in Table 2, the residuals between observed metallicity and $M_* - \Sigma_* - Z$ relation for all spaxels show smaller scatter than that of the $\Sigma_* - Z$ relation as expected.

Table 1
 p values (Significances) of PCOR For $\Sigma_* - Z$ and $M_* - Z$ with N2O2 Metallicity Index.

p	$\Sigma_* - Z$	$M_* - Z$
Pearson	0.746	0.668
Spearman	0.798	0.684
Kendall	0.579	0.441

In the *top* panels of Figure 3, we show the comparisons between the observed metallicity derived with N2O2 index and our best-fit $\Sigma_* - Z$ as well as $M_* - \Sigma_* - Z$ relations. The contours cover the metallicities for 85% of all spaxels, and the solid, unity lines are overplotted for eye guidance. These black dashed lines show the scatters for all spaxels, which are 0.096 dex for $\Sigma_* - Z$ relation, while are 0.070 dex for $M_* - \Sigma_* - Z$ relation. The mean values μ_{all} and standard deviation (scatters) σ_{all} for residuals ($\Delta 12 + \log(\text{O}/\text{H}) = 12 + \log(\text{O}/\text{H}) - 12 + \log(\text{O}/\text{H})_{\text{FIT}}$) are shown in the legends. Note that the scatter σ_{all} in $M_* - \Sigma_* - Z$ relation is significantly smaller than the value in the $\Sigma_* - Z$ relation. When the global stellar mass is taken into account, the scatter of the metallicity scaling relation is reduced by 27% for N2O2 index. This result means that above one quarter of the total scatter in $\Sigma_* - Z$ relation is due to the systematic effect with M_* , while the rest scatter (0.07 dex) is caused by other galactic parameters and/or intrinsic scatter (0.04 dex, N2O2) in metallicity calibration. This tight $M_* - \Sigma_* - Z$ relation extends over three orders of magnitude in the global stellar mass, nearly four orders of magnitude in the mass surface density, a factor of 6 in metallicity with N2O2 index.

In the *bottom* panels of Figure 3, we show the same relations but for massive galaxies. We note that the scatter in $\Sigma_* - Z$ relation is 0.068 dex, while reduced slightly to 0.061 dex in $M_* - \Sigma_* - Z$ relation. The much smaller reduction in scatter, less than 0.01 dex, suggests that the local metallicity distribution in massive galaxies probably has no or much weak dependence on their global stellar masses.

4. DISCUSSION

4.1. Comparison with Previous Studies

In this work, we analyze the dependence of metallicity on local stellar mass surface density and global stellar mass in a sample of 1122 SFGs from the MaNGA survey. Figure 2 shows that the metallicity increases largely with increasing M_* (or Σ_*) at a fixed Σ_* (or M_*) value. Furthermore, we perform PCOR analyses to accurately determine the strength of these correlations. From Table 1, we note that the significance p values for $M_* - Z$ and $\Sigma_* - Z$ are both prominent, indicating the importance of the roles that local Σ_* and global stellar mass play in determining the local metallicity. However, all of the p values for $\Sigma_* - Z$ are slightly larger than those for $M_* - Z$, suggesting that the local stellar mass surface density is more closely related to the local metallicity than to the galaxy stellar mass.

In the previous studies, some global galaxy properties, such as SFR, specific SFR, $D_n(4000)$ and gas fraction are introduced in order to explain the large scatter in global MZR. Mannucci et al. (2010) determined the metallicity with N2 and R23 (Nagao et al. 2006) indices, and defined a new quantity $\mu_\alpha = \log(M_*) - \alpha \log(\text{SFR})$ to reduce the scatter in MZR for local galaxies, resulting in a scatter of 0.05 dex in FMR. Andrews & Martini (2013) found the scatter in FMR to be about 0.13 dex, where the metallicity is calculated from the electron temperature T_e . Similarly, for the local $\Sigma_* - Z$ relation, although Barrera-Ballesteros et al. (2016) suggested that the $\Sigma_* - Z$ relation is largely independent of the galaxy's total stellar mass M_* except at low stellar mass ($\log(M_*/M_\odot) < 9.5$) and high specific SFR, they found a scatter of about 0.08 dex for the O3N2 estimator. In this work, we establish a new relation (Equation 4), which is a modification of the MZR in Moustakas et al. (2011), to reinvestigate the local $\Sigma_* - Z$ relation. We further take into account the contribution from the global M_* , and extend the Equation 4 to Equation 5 to reproduce the observed metallicity. As expected, the scatter in the $M_* - \Sigma_* - Z$ relation for all spaxels is significantly reduced. However, if excluding the low-mass ($\log(M_*/M_\odot) < 9.5$) galaxies in the previous analyses, we find the reductive scatter from $\Sigma_* - Z$ to $M_* - \Sigma_* - Z$ relation is much smaller. In Figure 6 of Appendix, we also plot the residuals between observed metallicity and the best fitted $\Sigma_* - Z$ relations as a function of stellar mass for each metallicity index. The median values of the residuals with O3N2 (*middel* panel) are in very good agreement with the results shown in the Fig.8 of Barrera-Ballesteros et al. (2016). We also note that, at the low stellar mass end, the $\Sigma_* - Z$ relations with these three calibrators can not ideally reproduce the observed metallicities. As a result, for massive galaxies, our results are mostly consistent with the finding in Barrera-Ballesteros et al. (2016), while for low-mass galaxies, the significantly suppressed scatters, from $\Sigma_* - Z$ to $M_* - \Sigma_* - Z$ relations, indicate that the global stellar mass has a nonnegligible effect on the local metallicity distribution of galaxies.

4.2. Residuals in the $M_* - \Sigma_* - Z$ Relation

Although the scatter in the $M_* - \Sigma_* - Z$ relation (Figure 3) is relatively small, the dependence of residuals on other galaxy properties is worth investigating, which promises to provide implications on further reducing the scatter of the metallicity scaling relations. For the radial bin sample used in Section 3.2 and Section 3.3, we calcu-

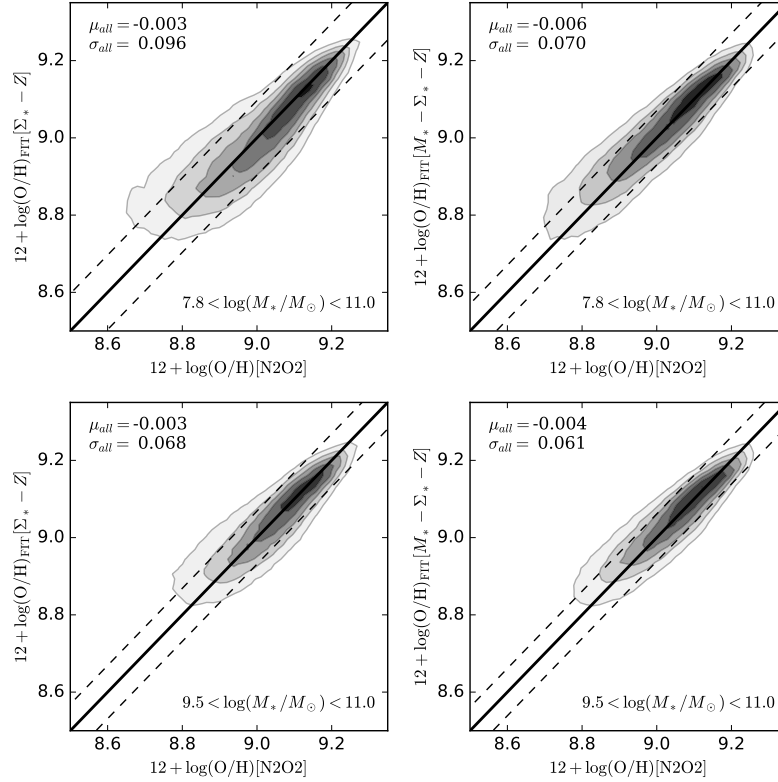


Figure 3. The comparisons between the observed metallicity with N2O2 index and our best-fitted $\Sigma_* - Z$ (left) and $M_* - \Sigma_* - Z$ (right) relations for all galaxies (top: $7.8 < \log(M_*/M_\odot) < 11.0$) and massive galaxies (bottom: $9.5 < \log(M_*/M_\odot) < 11.0$). The contours cover the metallicities for 85% of all spaxels. The mean value μ_{all} and standard deviation (scatter) σ_{all} for residuals ($\Delta 12 + \log(O/H)$) are shown in the legends. The solid lines indicate equality between the observed metallicity and best-fitted metallicity. These black dashed lines show the scatters for all spaxels, which are also shown in the legends.

Table 2
The Best-fitted Results For $\Sigma_* - Z$ and $M_* - \Sigma_* - Z$ Relations Based on N2O2 Metallicity Index.

$\log(M_*/M_\odot)$	[7.8, 11.0]		[9.5, 11.0]	
Parameters	$\Sigma_* - Z$	$M_* - \Sigma_* - Z$	$\Sigma_* - Z$	$M_* - \Sigma_* - Z$
$12 + \log(O/H)_o$	9.267 ± 0.018	9.320 ± 0.027	9.267 ± 0.018	9.333 ± 0.032
μ_{M_*}	–	0.406 ± 0.107	–	0.824 ± 0.467
$\log(M_{TO})$	–	9.385 ± 0.140	–	9.016 ± 0.314
γ_{M_*}	–	1.062 ± 0.130	–	0.973 ± 0.576
μ_{Σ_*}	0.350 ± 0.088	0.705 ± 0.302	0.334 ± 0.095	0.900 ± 0.525
$\log(\Sigma_{TO})$	8.050 ± 0.068	7.598 ± 0.349	8.082 ± 0.088	7.362 ± 0.604
γ_{Σ_*}	1.010 ± 0.193	0.538 ± 0.126	0.905 ± 0.189	0.476 ± 0.129
μ_{bin}	-0.0084	0.0001	-0.0009	-0.0002
σ_{bin}	0.0968	0.0638	0.059	0.052
μ_{all}	-0.0038	-0.0061	-0.003	-0.004
σ_{all}	0.0965	0.0702	0.068	0.061

Notes: The $12 + \log(O/H)_o$, μ_{M_*} , $\log(M_{TO})$, γ_{M_*} , μ_{Σ_*} , $\log(\Sigma_{TO})$ and γ_{Σ_*} are free parameters in $\Sigma_* - Z$ relation (Equation 4) and $M_* - \Sigma_* - Z$ relation (Equation 5). The μ_{bin} and σ_{bin} are the mean values and scatters for distributions of residuals between our radial bin sample and $\Sigma_* - Z$ or $M_* - \Sigma_* - Z$ relation, while the μ_{all} and σ_{all} are the mean values and scatters for all spaxel data. Our radial bin sample contain the median values of Σ_* , local SFRs and metallicities in the bin regions with $\Delta R/R_e = 0.3$ for each galaxy, see detail in Section 3.2.

late the difference between the observed metallicity and the one derived from the best-fit curves for the $M_* - \Sigma_* - Z$ relation using N2O2 index. In Figure 4, we show these residuals ($\Delta 12 + \log(\text{O}/\text{H})$) as a function of M_* , Σ_* , local SFR surface density (Σ_{SFR}), local D_{n4000} , the concentration index C (defined as the ratio R_{90}/R_{50}), and the gravitational potential ($\Phi = M_*/R_e$) (D’Eugenio et al. 2018). The black points represent the residuals for radial bin sample, the blue lines represent the median residual values for ten bins of each parameter, and the errorbars represent the 16% – 84% range of the binned distributions. The black solid lines depict the zero-residual locus.

We find that the median residuals with respect to M_* , Σ_* and Σ_{SFR} approximate zero consistently, an indication that the residuals do not systematically correlate with M_* , Σ_* and Σ_{SFR} . The result suggests that the local metallicity is nearly independent on local SFR at a fixed M_* and Σ_* , indicating that the so-called ‘local’ FMR vanished potentially, a conclusion consistent with previous studies (e.g. Sánchez et al. 2013; Barrera-Ballesteros et al. 2018). For spiral galaxies in the local universe, Leroy et al. (2008) have demonstrated that the gas depletion time ($\Sigma_{\text{gas}}/\Sigma_{\text{SFR}}$) is nearly constant based on molecular and atomic gas. The growth of local stellar mass surface density is mostly the product of consumption for local gas, while the global stellar mass is also affected by the transformation in global outflow and inflow. Furthermore, for massive galaxies, the $\Sigma_* - Z$ relation can also successfully reproduce the global MZR, which has been studied in some works (e.g. Barrera-Ballesteros et al. 2016; Sánchez et al. 2017), and then lead to the no or weak dependence of MZR on SFR. However, it should be noted that the hydrogen recombination lines, like $\text{H}\alpha$ and $\text{H}\beta$, are only sensitive to the shortest timescale (≤ 20 Myr) of star formation (Kennicutt 1998), which means that we get an instantaneous SFR estimation, instead of the previous star formation history. For massive galaxies, the majority of galaxies in this work, the local metallicity is largely independent on the local instantaneous star formation, since their long star formation history and normal star formation activities at the present day. For low-mass metal-poor galaxies, the dependence of global MZR on SFR might appear (e.g. Ly et al. 2016, Gao et al. 2018, submitted), because of their much more intense star formation activities and younger stellar populations. In the future, we will further check the existence of $M_* - \Sigma_* - Z$ relation, as well as its dependence on SFR surface density for the low-mass metal-poor SFGs based on the IFS data.

However, the residuals seemly show a weak correlation with D_{n4000} . With increasing D_{n4000} , the absolute values of residuals decrease when $D_{\text{n4000}} < 1.35$. The residuals are negative when $D_{\text{n4000}} < 1.25$, and are positive when $1.25 < D_{\text{n4000}} < 1.50$. These results indicate that our $M_* - \Sigma_* - Z$ relation overestimate the metallicity for very young ($\lesssim 0.25$ Gyr) galactic regions (Kauffmann et al. 2003), but underestimate the metallicity for galactic regions with an older stellar age. Lian et al. (2015) found that the metallicity is positive correlated to D_{n4000} , which indicates that galaxies with older stellar ages have higher metallicities. Furthermore, we also find that the residuals for concentration index C and gravitational potential Φ are nearly zero, meaning that the local metallicity may be independent on the

galaxy concentration and average gravitational potential. Recently, Wang et al. (2017) have demonstrated that the local metallicity also depends on the assembly modes of galaxies. In the sense that higher Σ_* (denser) regions, located in the inner regions of galaxies with an “outside-in” assembly mode, have higher metallicity and lower D_{n4000} than those galaxies with an “inside-out” mode. This may lead to additional scatter in $M_* - \Sigma_* - Z$ relation. In the future, we expect to further reduce the scatter in $M_* - \Sigma_* - Z$ relation by considering the different assembly modes of galaxies.

4.3. The Impact of Metallicity Calibrators

Apart from the N2O2 index used in the main text, we also estimate the metallicity with O3N2 and N2 diagnostics (see Appendix) to check whether our primary results are independent on the different metallicity estimators. The O3N2 and N2 calibrators are anchored by the “direct method” with electron temperature proposed by Marino et al. (2013), while the N2O2 calibrator is constructed by comparing the line ratios with photo-ionization models (Kewley & Dopita 2002). However, it is well known that these two procedures will lead to a relatively non-negligible difference in metallicity estimation (Morisset et al. 2016). Pettini & Pagel (2004) and López-Sánchez et al. (2011) have clearly shown that, when using the O3N2 and N2 diagnostics, the regions with higher ionization degree tend to have lower oxygen abundances. In particular, the N2O2 diagnostic is subject to variations in nitrogen-to-oxygen abundance ratio (N/O) ratios and temperature, and is sensitive to metallicity only for $Z > 8.3$ (Dopita et al. 2000, 2013; Pérez-Montero et al. 2016).

In Figure 2 and 5, we note that the metallicity with N2O2 index covers a wide range about 0.6 dex, while a narrow range less than 0.3 dex with N2 index, since the saturation that N2 suffered in the high-metallicity region. In addition, as shown in Figure 6, the absolute values of residual values increase with decreasing stellar mass, regardless the calibrator, while the absolute values of the residuals using O3N2 and N2 are systematically smaller than the N2O2 calibrator. Despite this, we find the trend, that the local metallicity increases with M_* (or Σ_*) at a fixed Σ_* (or M_*), is similar to the result with N2O2 index. In Figure 7 and 8, the scatters are also reduced by about 19% and 25% from $\Sigma_* - Z$ to $M_* - \Sigma_* - Z$ relations with O3N2 and N2 indices, respectively. Nevertheless, if excluding these low-mass galaxies, the reduced scatters are much smaller, which is consistent with the result with N2O2 index.

4.4. Implications of the $M_* - \Sigma_* - Z$ Relation

In Section 3, we find that a tight correlation exists between the global stellar mass, the local stellar mass surface density and the local metallicity, especially for low-mass star-forming galaxies, in which the metallicity increases with M_* and Σ_* in a systematic way. The local metallicities are mainly determined by the metals produced in the past, the metal loss by galactic outflows (Barrera-Ballesteros et al. 2018) or AGN feedback (Wylezalek et al. 2017), and the metal dilution by cold gas inflows. The local stellar mass surface density is a result of the local galactic stellar assembly history (Yozin &

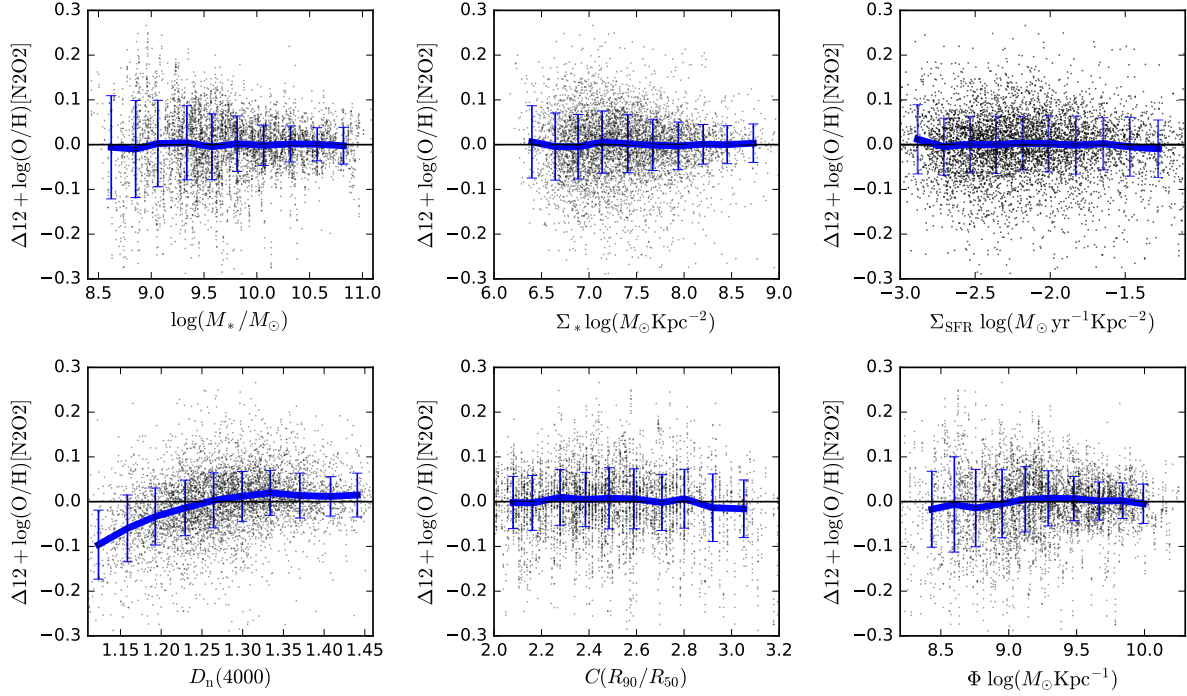


Figure 4. Residuals ($\Delta 12 + \log(\text{O}/\text{H})$) between observed metallicities and best-fitted $M_* - \Sigma_* - Z$ relation, for radial bin sample, with respect to the total stellar mass, local stellar mass surface density, local SFR surface density, local $D_n 4000$, concentration index C and average potential ($\Phi = M_*/R_e$). The black points represent the residual values for radial bin sample, the blue line-connected points represent the median residual values for 10 bins, and corresponding errorbars represent the 16% – 84% range in their distributions, respectively. The black solid lines represent zero-scatter in the $M_* - \Sigma_* - Z$ relation.

Bekki 2016; Goddard et al. 2017a,b; Jones et al. 2017), the strong correlation for $\Sigma_* - Z$ can be naturally explained by noticing that the higher Σ_* (denser) regions usually locate in the inner region of galaxies (Johnston et al. 2017), which have longer star formation history than the less dense regions with lower Σ_* (Ibarra-Medel et al. 2016).

Furthermore, the global stellar mass reflects the assembly of the stellar mass and the depth of the potential wells, which dominates the infall of metal-poor gas and the outflows of metal-rich gas (Peeples & Shankar 2011; Pan et al. 2015; Cheung et al. 2016; Lian et al. 2018). As proposed by Tremonti et al. (2004) and Lian et al. (2018), the deep gravitational potential wells of massive galaxies retain the processed metals, leading to a higher local metallicity than less massive galaxies even at a similar Σ_* . In general, less massive galaxies are expected to be more efficient in diluting the metal-rich gas, caused by metal-poor gas inflows, and removing the metal-rich gas by stronger galactic outflows (Chisholm et al. 2018), due to their shallower gravitational potential wells and longer timescale for the inflow. Compared with these high-mass galaxies, low-mass galaxies are less efficient in converting gas into stars, which is the so-called ‘downsizing’ scenario (Thomas et al. 2010), and thus have the relatively higher gas fraction ($\Sigma_{\text{gas}}/\Sigma_*$). Barrera-Ballesteros et al. (2018) also argued that the gas fraction decreases tightly with the increasing local stellar mass surface density. For galaxies with higher stellar mass and higher local stellar mass surface density, the star formation activity becomes relatively weaker because of the lower gas fraction. Recently, Chisholm et al. (2018) has suggested that it

is easier to significantly remove the metals by stronger galactic outflows in low-mass galaxies than in massive galaxies. Nevertheless, we should notice that Chisholm et al. (2018) just derived the outflow properties for seven galaxies, which cover a wide range of stellar mass but lack the range of $7.5 \leq \log(M_*/M_\odot) \leq 9.0$. In brief, the dependence of local stellar mass surface density – local metallicity relation on global stellar mass is pronounced for low-mass galaxies, since their shallower gravitational potential wells, while is more or less weaker for massive galaxies.

5. SUMMARY

In this work, we have used the IFS data from the MaNGA survey to investigate the global stellar mass – local stellar mass surface density – metallicity relation, and the strengths of their correlation with metallicity in star-forming galaxies. In total, we select 1122 star-forming galaxies with about 750,000 spaxels in star-forming regions as our sample. We have determined the local metallicities with the N2O2 diagnostic. The local stellar mass surface densities are derived from the best-fit results given by STARLIGHT, and the SFR surface density are estimated from $\text{H}\alpha$ luminosities. The main results and conclusions of this paper are summarized as follows.

- In agreement with previous studies, the metallicity increases steeply with increasing surface stellar mass density at a fixed stellar mass. Similarly, at a fixed surface stellar mass density, the metallicity increases strongly with increasing stellar mass at low

mass end, while this trend becomes less obvious at high mass end (Figure 2). Performing partial correlation analyses on M_* , Σ_* and Z (Table 1), we find that the p values for the correlations of $M_* - Z$ and $\Sigma_* - Z$ to be large, indicating that metallicity is partially dependent on both global stellar mass and local mass surface density. However, all p values for the $\Sigma_* - Z$ relation are slightly larger than those for the $M_* - Z$ relation, indicating that the local metallicity Z correlates with Σ_* more strongly than M_* .

- We establish the $\Sigma_* - Z$ relation (Equation 4) following the relation in Moustakas et al. (2011), and extend the $\Sigma_* - Z$ relation to a new $M_* - \Sigma_* - Z$ relation (Equation 5, Figure 3). Compared to $\Sigma_* - Z$ relation, the scatter in the $M_* - \Sigma_* - Z$ relation is reduced by about 30% for galaxies with $7.8 < \log(M_*/M_\odot) < 11.0$, while the reduced scatter is much smaller when excluding the low-mass ($\log(M_*/M_\odot) < 9.5$) galaxies, suggesting that the $M_* - \Sigma_* - Z$ relation is a more universal and fundamental relation than $M_* - Z$ and $\Sigma_* - Z$ relations for those low-mass galaxies.
- We find the residuals in the best-fitted $M_* - \Sigma_* - Z$ relation to be possibly correlated with the D_n4000 (Figure 4). When including the contribution of the SFR, we find that the local metallicity is largely independent on the local SFR surface density at a fixed M_* and Σ_* , indicating the lack of so-called ‘local’ FMR, consistent with previous studies.

We emphasize that our basic results do not depend on the different metallicity estimators (e.g. O3N2, N2, see Appendix). The local metallicity can be determined well with the global stellar mass and local stellar mass surface density, suggesting that the local metallicity is primarily determined by both the local galactic stellar mass assembly history and the global stellar mass assembly history. We interpret our result as the combination of the produced metals in the local star formation history and the metal loss due to the galactic winds from the galactic potential wells. Furthermore, the remaining scatter in the $M_* - \Sigma_* - Z$ relation may be contributed by the local D_n4000 .

We thank the referee for her/his constructive comments. We thank Jianhui Lian for useful discussion on the manuscript. This work is supported by the National Key R&D Program of China (2015CB857004, 2016YFA0400702, 2017YFA0402600), and the National Natural Science Foundation of China (NSFC, Nos. 11320101002, 11421303, and 11433005). Enci Wang acknowledges the support from the Youth Innovation Fund by University of Science and Technology of China (No. WK2030220019) and the China Postdoctoral Science Foundation funded project (No. BH2030000040). Guilin Liu acknowledges the support from the National Thousand Young Talents Program of China.

Funding for the Sloan Digital Sky Survey IV has been provided by the Alfred P. Sloan Foundation, the U.S. Department of Energy Office of Science, and the Participating Institutions. SDSS acknowledges support and

resources from the Center for High-Performance Computing at the University of Utah. The SDSS web site is www.sdss.org.

SDSS is managed by the Astrophysical Research Consortium for the Participating Institutions of the SDSS Collaboration including the Brazilian Participation Group, the Carnegie Institution for Science, Carnegie Mellon University, the Chilean Participation Group, the French Participation Group, Harvard-Smithsonian Center for Astrophysics, Instituto de Astrofísica de Canarias, The Johns Hopkins University, Kavli Institute for the Physics and Mathematics of the Universe (IPMU) / University of Tokyo, Lawrence Berkeley National Laboratory, Leibniz Institut für Astrophysik Potsdam (AIP), Max-Planck-Institut für Astronomie (MPIA Heidelberg), Max-Planck-Institut für Astrophysik (MPA Garching), Max-Planck-Institut für Extraterrestrische Physik (MPE), National Astronomical Observatories of China, New Mexico State University, New York University, University of Notre Dame, Observatorio Nacional / MCTI, The Ohio State University, Pennsylvania State University, Shanghai Astronomical Observatory, United Kingdom Participation Group, Universidad Nacional Autónoma de México, University of Arizona, University of Colorado Boulder, University of Oxford, University of Portsmouth, University of Utah, University of Virginia, University of Washington, University of Wisconsin, Vanderbilt University, and Yale University.

REFERENCES

- Abazajian, K. N., Adelman-McCarthy, J. K., Agüeros, M. A., et al. 2009, *ApJS*, 182, 543
- Abolfathi, B., Aguado, D. S., Aguilar, G., et al. 2018, *ApJS*, 235, 42
- Alloin, D., Collin-Souffrin, S., Joly, M., & Vigroux, L. 1979, *A&A*, 78, 200
- Andrews, B. H., & Martini, P. 2013, *ApJ*, 765, 140
- Baldwin, A., Phillips, M. M., & Terlevich, R. 1981, *PASP*, 93, 817
- Barrera-Ballesteros, J. K., Sánchez, S. F., Heckman, T., Blanc, G. A., & Team, T. M. 2017, *ApJ*, 844, 80
- Barrera-Ballesteros, J. K., Heckman, T. M., Zhu, G. B., et al. 2016, *MNRAS*, 463, 2513
- Barrera-Ballesteros, J. K., Heckman, T., Sánchez, S. F., et al. 2018, *ApJ*, 852, 74
- Blanc, G. A., Kewley, L., Vogt, F. P. A., & Dopita, M. A. 2015, *ApJ*, 798, 99
- Blanton, M. R., Kazin, E., Muna, D., Weaver, B. A., & Price-Whelan, A. 2011, *AJ*, 142, 31
- Blanton, M. R., Bershad, M. A., Abolfathi, B., et al. 2017, *AJ*, 154, 28
- Bothwell, M. S., Maiolino, R., Peng, Y., et al. 2016, *MNRAS*, 455, 1156
- Bruzual, G., & Charlot, S. 2003, *MNRAS*, 344, 1000
- Bundy, K., Bershad, M. A., Law, D. R., et al. 2015, *ApJ*, 798, 7
- Calzetti, D., Armus, L., Bohlin, R. C., et al. 2000, *ApJ*, 533, 682
- Chabrier, G. 2003, *PASP*, 115, 763
- Cheung, E., Stark, D. V., Huang, S., et al. 2016, *ApJ*, 832, 182
- Chisholm, J., Tremonti, C., & Leitherer, C. 2018, *ArXiv e-prints*, arXiv:1808.10453
- Cid Fernandes, R., Mateus, A., Sodré, L., Stasińska, G., & Gomes, J. M. 2005, *MNRAS*, 358, 363
- D’Eugenio, F., Colless, M., Groves, B., Bian, F., & Barone, T. M. 2018, *MNRAS*, arXiv:1805.12131
- Dopita, M. A., Kewley, L. J., Heisler, C. A., & Sutherland, R. S. 2000, *ApJ*, 542, 224
- Dopita, M. A., Sutherland, R. S., Nicholls, D. C., Kewley, L. J., & Vogt, F. P. A. 2013, *ApJS*, 208, 10
- Drory, N., MacDonald, N., Bershad, M. A., et al. 2015, *AJ*, 149, 77
- Edmunds, M. G., & Pagel, B. E. J. 1984, *MNRAS*, 211, 507

- Ellison, S. L., Patton, D. R., Simard, L., & McConnell, A. W. 2008, *ApJL*, 672, L107
- Gao, Y.-L., Lian, J.-H., Kong, X., et al. 2017, *Research in Astronomy and Astrophysics*, 17, 041
- Garnett, D. R., & Shields, G. A. 1987, *ApJ*, 317, 82
- Goddard, D., Thomas, D., Maraston, C., et al. 2017a, *MNRAS*, 465, 688
- . 2017b, *MNRAS*, 466, 4731
- Hu, N., Su, S.-S., & Kong, X. 2016, *Research in Astronomy and Astrophysics*, 16, 006
- Hummer, D. G., & Storey, P. J. 1987, *MNRAS*, 224, 801
- Ibarra-Medel, H. J., Sánchez, S. F., Avila-Reese, V., et al. 2016, *MNRAS*, 463, 2799
- Johnston, E. J., Häußler, B., Aragón-Salamanca, A., et al. 2017, *MNRAS*, 465, 2317
- Jones, A., Kauffmann, G., D’Souza, R., et al. 2017, *A&A*, 599, A141
- Kauffmann, G., Heckman, T. M., White, S. D. M., et al. 2003, *MNRAS*, 341, 33
- Kehrig, C., Pérez-Montero, E., Vílchez, J. M., et al. 2013, *MNRAS*, 432, 2731
- Kendall, M. G. 1938, *Biometrika*, 30, 81
- Kennicutt, Jr., R. C. 1998, *ARA&A*, 36, 189
- Kewley, L. J., & Dopita, M. A. 2002, *ApJS*, 142, 35
- Kewley, L. J., Dopita, M. A., Sutherland, R. S., Heisler, C. A., & Trevena, J. 2001, *ApJ*, 556, 121
- Kewley, L. J., & Ellison, S. L. 2008, *ApJ*, 681, 1183
- Kobulnicky, H. A., & Kewley, L. J. 2004, *ApJ*, 617, 240
- Lequeux, J., Peimbert, M., Rayo, J. F., Serrano, A., & Torres-Peimbert, S. 1979, *A&A*, 80, 155
- Leroy, A. K., Walter, F., Brinks, E., et al. 2008, *AJ*, 136, 2782
- Li, C., Wang, E., Lin, L., et al. 2015, *ApJ*, 804, 125
- Lian, J., Thomas, D., Maraston, C., et al. 2018, *MNRAS*, 474, 1143
- Lian, J. H., Li, J. R., Yan, W., & Kong, X. 2015, *MNRAS*, 446, 1449
- Lin, Z., Hu, N., Kong, X., et al. 2017, *ApJ*, 842, 97
- Liu, G., Calzetti, D., Hong, S., et al. 2013, *ApJL*, 778, L41
- López-Sánchez, Á. R., Mesa-Delgado, A., López-Martín, L., & Esteban, C. 2011, *MNRAS*, 411, 2076
- Ly, C., Malkan, M. A., Nagao, T., et al. 2014, *ApJ*, 780, 122
- Ly, C., Malkan, M. A., Rigby, J. R., & Nagao, T. 2016, *ApJ*, 828, 67
- Mannucci, F., Cresci, G., Maiolino, R., Marconi, A., & Gnerucci, A. 2010, *MNRAS*, 408, 2115
- Marino, R. A., Rosales-Ortega, F. F., Sánchez, S. F., et al. 2013, *A&A*, 559, A114
- Markwardt, C. B., Swank, J. H., Barthelmy, S. D., et al. 2009, *The Astronomer’s Telegram*, 2258
- Moran, S. M., Heckman, T. M., Kauffmann, G., et al. 2012, *ApJ*, 745, 66
- Morisset, C., Delgado-Inglada, G., Sánchez, S. F., et al. 2016, *A&A*, 594, A37
- Moustakas, J., Zaritsky, D., Brown, M., et al. 2011, *ArXiv e-prints*, arXiv:1112.3300
- Nagao, T., Maiolino, R., & Marconi, A. 2006, *A&A*, 459, 85
- Pan, Z., Li, J., Lin, W., et al. 2015, *ApJL*, 804, L42
- Pearson, K. 1895, *Proceedings of the Royal Society of London Series I*, 58, 240
- Peeples, M. S., & Shankar, F. 2011, *MNRAS*, 417, 2962
- Pérez-Montero, E., García-Benito, R., Vílchez, J. M., et al. 2016, *A&A*, 595, A62
- Pettini, M., & Pagel, B. E. J. 2004, *MNRAS*, 348, L59
- Raimann, D., Storch-Bergmann, T., Bica, E., Melnick, J., & Schmitt, H. 2000, *MNRAS*, 316, 559
- Rosales-Ortega, F. F., Kennicutt, R. C., Sánchez, S. F., et al. 2010, *MNRAS*, 405, 735
- Rosales-Ortega, F. F., Sánchez, S. F., Iglesias-Páramo, J., et al. 2012, *ApJL*, 756, L31
- Salim, S., Lee, J. C., Ly, C., et al. 2014, *ApJ*, 797, 126
- Salim, S., Rich, R. M., Charlot, S., et al. 2007, *ApJS*, 173, 267
- Salpeter, E. E. 1955, *ApJ*, 121, 161
- Sánchez, S. F., Kennicutt, R. C., Gil de Paz, A., et al. 2012, *A&A*, 538, A8
- Sánchez, S. F., Rosales-Ortega, F. F., Jungwiert, B., et al. 2013, *A&A*, 554, A58
- Sánchez, S. F., Pérez, E., Sánchez-Blázquez, P., et al. 2016, *RevMex*, 52, 171
- Sánchez, S. F., Barrera-Ballesteros, J. K., Sánchez-Menguiano, L., et al. 2017, *MNRAS*, 469, 2121
- Schlegel, D. J., Finkbeiner, D. P., & Davis, M. 1998, *ApJ*, 500, 525
- Sparre, M., & Springel, V. 2017, *MNRAS*, 470, 3946
- Speagle, J. S., Steinhardt, C. L., Capak, P. L., & Silverman, J. D. 2014, *ApJS*, 214, 15
- Spearman, C. 1904, *The American Journal of Psychology*, 15, 72
- Storch-Bergmann, T., Calzetti, D., & Kinney, A. L. 1994, *ApJ*, 429, 572
- Thomas, D., Maraston, C., Schawinski, K., Sarzi, M., & Silk, J. 2010, *MNRAS*, 404, 1775
- Tremonti, C. A., Heckman, T. M., Kauffmann, G., et al. 2004, *ApJ*, 613, 898
- Vazdekis, A., Ricciardelli, E., Cenarro, A. J., et al. 2012, *MNRAS*, 424, 157
- Vila-Costas, M. B., & Edmunds, M. G. 1992, *MNRAS*, 259, 121
- Wang, E., Kong, X., & Pan, Z. 2018, *ArXiv e-prints*, arXiv:1808.05929
- Wang, E., Kong, X., Wang, H., et al. 2017, *ApJ*, 844, 144
- Wylezalek, D., Schnorr Müller, A., Zakamska, N. L., et al. 2017, *MNRAS*, 467, 2612
- Yan, R., Tremonti, C., Bershady, M. A., et al. 2015, *The Astronomical Journal*, 151, 8
- Yan, R., Bundy, K., Law, D. R., et al. 2016, *The Astronomical Journal*, 152, 197
- Yang, G., Chen, C.-T. J., Vito, F., et al. 2017, *ApJ*, 842, 72
- Yates, R. M., Kauffmann, G., & Guo, Q. 2012, *MNRAS*, 422, 215
- Yozin, C., & Bekki, K. 2016, *MNRAS*, 460, 3968
- Zaritsky, D., Kennicutt, Jr., R. C., & Huchra, J. P. 1994, *ApJ*, 420, 87
- Zhang, K., Yan, R., Bundy, K., et al. 2017, *MNRAS*, 466, 3217
- Zhu, G. B., Barrera-Ballesteros, J. K., Heckman, T. M., et al. 2017, *MNRAS*, 468, 4494

APPENDIX

THE METALLICITY CALCULATION WITH O3N2 AND N2 DIAGNOSTICS

The diagnostic O3N2 index (Alloin et al. 1979) is defined as

$$\text{O3N2} \equiv \log\left(\frac{[\text{O III}]\lambda 5007}{\text{H}\beta} \times \frac{\text{H}\alpha}{[\text{N II}]\lambda 6583}\right). \quad (\text{A1})$$

The empirical calibration of O3N2 diagnostic for the specific purpose of calculating metallicity, improved by Marino et al. (2013), is

$$12 + \log(\text{O}/\text{H}) = 8.505 - 0.221 \times \text{O3N2} \quad (\text{A2})$$

with O3N2 ranging from -1.1 to 1.7 . The typical error for the metallicity calibration with the O3N2 diagnostic is 0.08 dex.

The diagnostic N2 index (Storchi-Bergmann et al. 1994; Raimann et al. 2000) is defined as

$$\text{N2} \equiv \log([\text{N II}]\lambda 6583/\text{H}\alpha), \quad (\text{A3})$$

and the metallicity calibration relation, derived by Marino et al. (2013), is given by

$$12 + \log(\text{O}/\text{H}) = 8.667 + 0.455 \times \text{N2}, \quad (\text{A4})$$

with an average uncertainty of 0.09 dex, where the N2 index is between -1.6 and -0.2 .

THE PCOR ANALYSIS, Σ_* – Z AND M_* – Σ_* – Z RELATIONS WITH O3N2 AND N2 INDICES

Table 3
 p values (Significances) of PCOR Based on O3N2 and N2 Metallicity Indices.

p	O3N2		N2	
	$\Sigma_* - Z$	$M_* - Z$	$\Sigma_* - Z$	$M_* - Z$
Pearson	0.699	0.603	0.665	0.627
Spearman	0.746	0.613	0.704	0.680
Kendall	0.545	0.405	0.485	0.462

Table 4
The Best-fitted Results For $\Sigma_* - Z$ and $M_* - \Sigma_* - Z$ Relations Based on O3N2 and N2 Metallicity Indices.

Parameters	O3N2				N2			
	[7.8, 11.0]		[9.5, 11.0]		[7.8, 11.0]		[9.5, 11.0]	
	$\Sigma_* - Z$	$M_* - \Sigma_* - Z$	$\Sigma_* - Z$	$M_* - \Sigma_* - Z$	$\Sigma_* - Z$	$M_* - \Sigma_* - Z$	$\Sigma_* - Z$	$M_* - \Sigma_* - Z$
$12 + \log(\text{O}/\text{H})_{\text{O}}$	8.575 ± 0.009	8.565 ± 0.009	8.575 ± 0.009	8.558 ± 0.007	8.595 ± 0.009	8.571 ± 0.003	8.590 ± 0.008	8.568 ± 0.005
μM_*	–	0.148 ± 0.044	–	0.397 ± 0.290	–	0.249 ± 0.050	–	0.222 ± 0.668
$\log(M_{\text{T O}})$	–	9.523 ± 0.133	–	9.083 ± 0.306	–	9.310 ± 0.122	–	9.362 ± 1.876
γM_*	–	1.190 ± 0.189	–	1.261 ± 0.772	–	0.898 ± 0.085	–	0.913 ± 0.553
$\mu \Sigma_*$	0.265 ± 0.068	0.230 ± 0.077	0.250 ± 0.070	0.302 ± 0.100	0.345 ± 0.146	0.102 ± 0.018	0.300 ± 0.164	0.139 ± 0.037
$\log(\Sigma_{\text{T O}})$	7.755 ± 0.097	7.669 ± 0.165	7.738 ± 0.117	7.392 ± 0.204	7.315 ± 0.275	7.361 ± 0.052	7.214 ± 0.410	7.170 ± 0.104
$\gamma \Sigma_*$	0.925 ± 0.163	0.801 ± 0.167	0.905 ± 0.163	0.799 ± 0.136	0.75 ± 0.161	1.572 ± 0.186	0.702 ± 0.167	1.439 ± 0.191
μ_{bin}	–0.005	0.0004	–0.003	0.003	0.0026	0.0022	–0.002	–0.0001
σ_{bin}	0.0528	0.0390	0.0358	0.0332	0.0467	0.0320	0.0309	0.0252
μ_{all}	0.002	0.0018	0.0006	0.0027	0.0011	–0.0012	–0.003	–0.002
σ_{all}	0.0571	0.0465	0.0452	0.0424	0.0515	0.0385	0.0385	0.0332

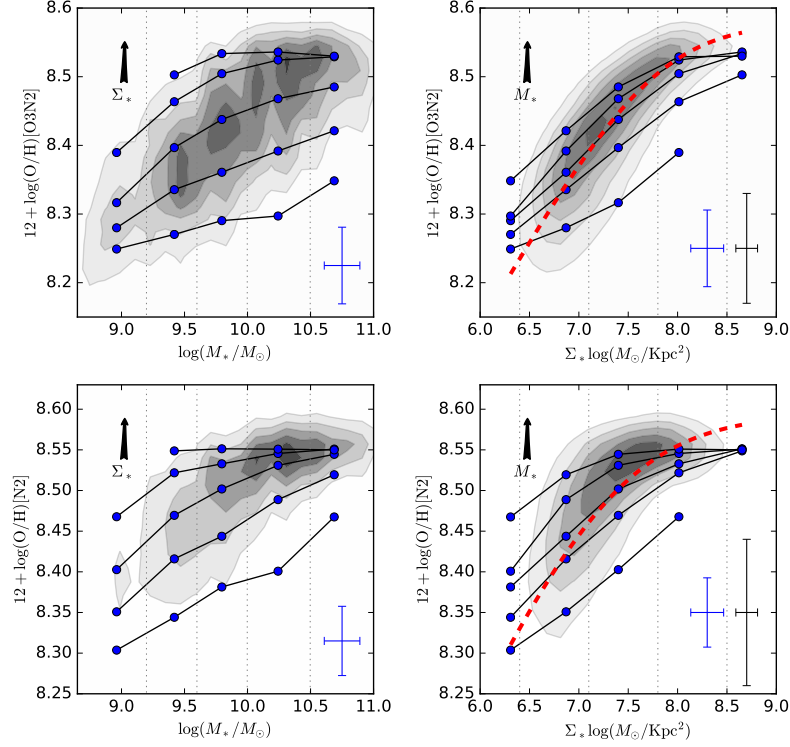


Figure 5. The metallicity distribution in M_* and Σ_* space based on O3N2 and N2 indices. The meaning of symbols is same as Figure 2.

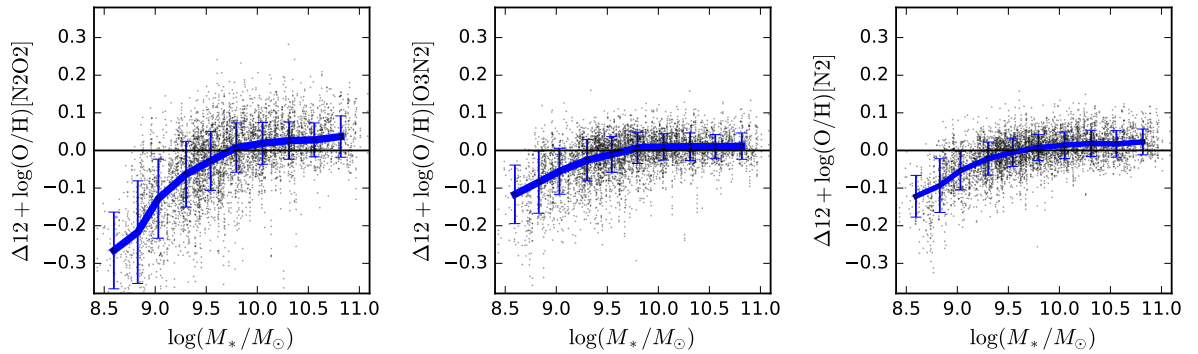


Figure 6. Residuals ($\Delta 12 + \log(\text{O}/\text{H})$) between observed metallicities and best-fitted $\Sigma_* - Z$ relation, for three metallicity calibrators, with respect to the total stellar mass. The black points represent the residual values for radial bin sample, the blue line-connected points represent the median residual values for 10 bins, and corresponding errorbars represent the 16% – 84% range in their distributions, respectively. The black solid lines represent zero-scatter in the $\Sigma_* - Z$ relation.

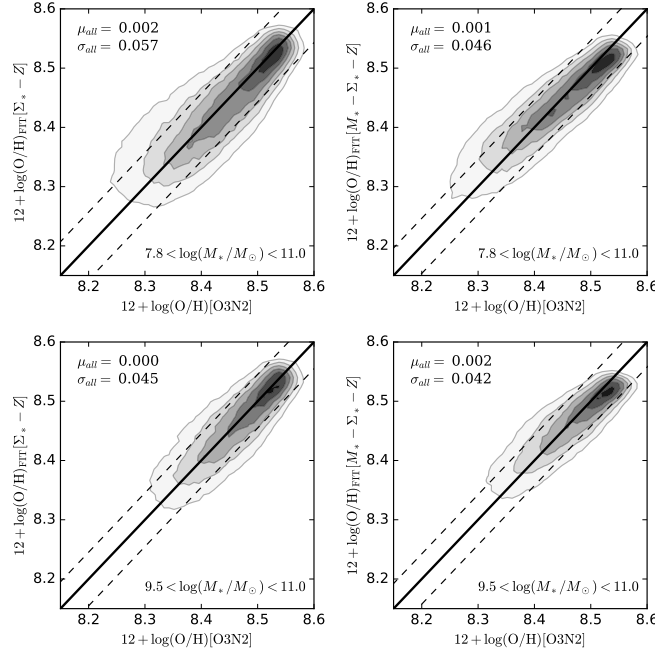


Figure 7. The comparisons between the observed metallicity with O3N2 index and our best-fitted $\Sigma_* - Z$ (left) and $M_* - \Sigma_* - Z$ (right) relations for all galaxies (top: $7.8 < \log(M_*/M_\odot) < 11.0$) and massive galaxies (bottom: $9.5 < \log(M_*/M_\odot) < 11.0$). The meaning of symbols is same as Figure 3.

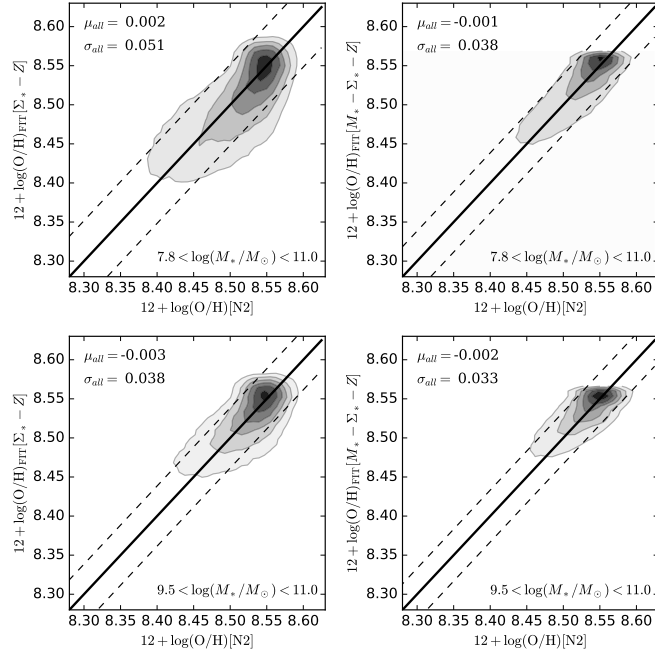


Figure 8. The comparisons between the observed metallicity with N2 index and our best-fitted $\Sigma_* - Z$ (left) and $M_* - \Sigma_* - Z$ (right) relations for all galaxies (top: $7.8 < \log(M_*/M_\odot) < 11.0$) and massive galaxies (bottom: $9.5 < \log(M_*/M_\odot) < 11.0$). The meaning of symbols is same as Figure 3.